

4-2019

Accuracy of Personalized 3-D Printed Phantoms for Radiotherapy Applications

Margaret Carey

Follow this and additional works at: https://repository.lsu.edu/honors_etd



Part of the [Astrophysics and Astronomy Commons](#)

Recommended Citation

Carey, Margaret, "Accuracy of Personalized 3-D Printed Phantoms for Radiotherapy Applications" (2019). *Honors Theses*. 268.

https://repository.lsu.edu/honors_etd/268

This Thesis is brought to you for free and open access by the Ogden Honors College at LSU Scholarly Repository. It has been accepted for inclusion in Honors Theses by an authorized administrator of LSU Scholarly Repository. For more information, please contact ir@lsu.edu.

**Accuracy of Personalized 3-D Printed Phantoms for
Radiotherapy Applications**

Undergraduate thesis under the direction of Dr. Wayne Newhauser

Department of Physics and Astronomy

Louisiana State University

by

Margaret Carey

(April 2019)

Acknowledgements:

I would like to thank my research advisor, Dr. Wayne Newhauser, for his guidance and support throughout the process of project. I thank my committee members Drs. Kenneth Matthews and Khoa Nguyen for their time and assistance while serving on my thesis defense committee.

This research was supported in part by the Tiger Athletic Foundation Honors Thesis Research Scholarship, the Department of Radiation Medicine at Oregon Health & Science University, the Bella Bowman Foundation, the Nuclear Regulatory Commission, and LSU Office of Research and Development.

A special thanks to Drs. Kyle Gallagher and Phillip Taddei as well as Mr. Hunter Tillery for their contribution of Bragg peak measurements. Thank you to Ms. Meagan Moore for her guidance throughout the process of creating the phantom, without which this project would not have been possible. Thank you to Dr. Niloufar Emami for her help with printing the gypsum slabs. I would also like to thank the members of our research group, especially William Donahue and Lydia Wilson, for their invaluable discussion and editing.

Finally, I would like to thank my family and Eli Bacilla for their support and encouragement through this new and challenging process of exploration.

This work is dedicated to the memory of Bella Bowman.

Table of Contents

ACKNOWLEDGEMENTS	ii
ABSTRACT	iv
CHAPTER 1	
1 INTRODUCTION	1
CHAPTER 2	
2 EXPERIMENTAL DESIGN AND METHODS	4
2.1 Pediatric Phantom	4
2.2 Bone Heterogeneities	9
CHAPTER 3	
3 RESULTS	13
3.1 Geometric Accuracy of Whole Body Phantom	13
3.2 Dosimetric Accuracy of Bone Heterogeneities.....	15
CHAPTER 4	
4 DISCUSSION	17
CHAPTER 5	
5 CONCLUSION	20
REFERENCES	22

Abstract

Cancer is the second-leading cause of death worldwide, and it is commonly treated with radiation therapy. Measurements are viewed as the gold standard for verifying the radiation dose deposition from a planned radiotherapy treatment. These measurements are typically performed in anthropomorphic phantoms with a population-averaged geometry. Not all patients, however, are well-represented by population-averaged geometries and require a more personalized approach. The purpose of this study was to determine the geometric and dosimetric accuracy of 3-d printed whole-body phantoms. To achieve this, we 3-d printed a phantom from a 3-d scan of an anthropomorphic phantom. We determined the geometric accuracy of the printed phantom compared to the reference phantom with dimensional measurements at corresponding locations. We investigated the dosimetric accuracy of 3-d-printed gypsum as a bone substitute material by measuring the water-equivalent thicknesses of gypsum slabs of selected physical thicknesses and compared them to that of bone. The results of this study demonstrated that it is possible to create 3-d printed phantoms with dimensional accuracy within $0.97 \text{ cm} \pm 0.12 \text{ cm}$ and $1.6\% \pm 0.2\%$ of a reference geometry and that it is possible to use 3-d printed gypsum as a bone substitute material. Together, 3-d printing personalized phantoms using gypsum as a bone model can be implemented to construct personalized phantoms, complete with accurate geometrical and dosimetric representation of the patient's anatomical uniqueness.

Chapter 1

Introduction

Cancer is the second leading cause of death in the world², and radiation therapy is commonly used for treatment³. In modern-day medicine, customizing every patient's treatment plan is becoming, more often than not, the default expectation in most fields. Though a standardized approach is followed in selecting treatment, each personalized treatment plan is according to the patient's unique situation (*e.g.*, tumor stage, location, size)³.

Cancer is a disease with many different treatment options (*e.g.*, surgery, chemotherapy, radiation therapy)². More than 50% of patients diagnosed with cancer will undergo some form of radiation therapy during their treatment process³. Radiation therapy works by inducing single- or double-strand DNA breaks in the cancerous cells, thus resulting in apoptosis of those cancerous cells⁴. The amount of energy per mass deposited into the body by radiation is known as the absorbed radiation dose. Absorbed radiation is affected by both host factors (*e.g.*, disease site, tumor size) and treatment factors (*e.g.*, radiation type, beam path in patient, etc.)⁵. The patient anatomy (*i.e.*, healthy and diseased tissues) is unique in every treatment case. Therefore, every treatment plan must be specified to accommodate for these unique factors.

Because surface geometry affects how the dose is distributed within the patient, treating patients with abnormal surface geometries (*e.g.*, patients with large superficial tumors, who have undergone mastectomies) necessitates a more personalized approach to treatment planning. Taking the patient's specific geometry into account during treatment planning generally improves the treatment efficacy.

Measurements are viewed as the gold standard for verifying the radiation dose deposition from a planned radiotherapy treatment. It is usually not practical, however, to measure the dose

delivered inside of a patient, and therefore phantoms are used as substitutes when measuring the energy deposited during radiation therapy treatment. One application of phantoms is in the development and testing of personalized strategies for targeting tumors. Commercial anthropomorphic phantoms are much like mannequins, but constructed with special materials to mimic tissue's dosimetric properties. These phantoms typically represent a standard, population-averaged geometry and are not personalized to the patient's unique anatomy. This is a major obstacle to accurately measuring the absorbed dose for patients with non-standard anatomies and tumors. One possible solution to this problem is 3-d-printed, personalized phantoms. This approach has successfully been used to print small portions of the body, such as a torso⁶ and head^{7,8}. There are many steps to create such phantoms, the first being describing the geometry to be printed.

There are multiple methods to generate printing instructions and perform the 3-d printing. Printing instructions can be created from different types of scans, such as optical scans of the patient's surface or computed tomography (CT) scans of the patient's surface and interior anatomy. Based on the type of scan performed, there are a variety of printing options. CT scans can be used to print both the internal and external geometry of the scanned person^{7,9}. Optical scans can be used to recreate the external geometry, by printing shells that can then be filled with different tissue-approximating materials for dosimetry purposes such as water or wax¹⁰. The external geometry of a personalized phantom serves to prevent surface irregularities from affecting the measured dose distribution. Using such a phantom with accurate external physical geometry facilitates interpretation of some aspects of the measured dose¹¹.

Three-dimensional printing capabilities are manifold, each suited to a specific purpose¹². In this work, we focused on two methods: fused deposition modeling (FDM) and binder jetting.

FDM stacks layers of heated material to build the 3-d model^{13, 14}. FDM is relatively inexpensive and fast, making it a popular method of 3-d printing. In the 3-d printing of phantoms, FDM offers a method for representing tissues and air cavities. Binder jetting involves applying chemical binding agents to layers of powder¹⁵. The binding agent causes the powder to solidify, leading to the production of a 3-d structure. The powders tend to have a high mass density, and therefore offer a means of modeling bone.

One aspect of 3-d printing that is attractive for creating personalized phantoms is the ability to print various mass densities. This enables accurate fabrication of electron densities in complicated geometries⁷. Applications of this technique include replicating human bone, soft tissue, and gas cavities in personalized phantoms. Madamesila *et al.* demonstrated that current 3-d printing technologies are limited by the inability to print varying infill densities in one single print¹². Previous attempts to model bone in 3-d printing projects used bone substitute plastics¹⁶⁻¹⁸, nylon models¹⁴, and other 3-d printing materials¹⁹. Advancements in 3-d printing technology have enabled the 3-d printing of gypsum (3DSystems, Zprinter 450, Rock Hill, SC, United States), which has a density similar to that of human bone¹⁹.

Other than the study performed by Moore and Newhauser²⁰, current studies on 3-d printing for radiotherapy applications are limited to partial 3-d prints of the body^{6, 7, 10, 17, 18}. At this stage of incorporating 3-d printing into radiotherapy treatment planning, full body 3-d printing has only narrowly been explored. There is more known, however, about representing proper density ranges in human phantoms. Proper dosimetric representation for bone has been attempted with many materials^{14, 16-19}, however, none have perfectly modeled the dosimetric properties of bone.

The purpose of this study was to determine the print accuracy of 3-d printed whole-body phantoms and to investigate gypsum as a bone-substitute material. We achieved this by replicating an anthropomorphic phantom using 3-d scanning and printing systems and studying the water equivalent thickness (WET) of 3-d printed gypsum slabs.

Chapter 2

Experimental Design/Methods

In this study, we investigated the dimensional accuracy of 3-d printing a phantom and the dosimetric properties of using high-density gypsum material to mimic cortical bone. First, we scanned a reference phantom and 3-d printed its image (Section 2.1.1 – 2.1.3). Next, we prepared the 3-d printed phantom to be filled with water for use as a personalized water-box phantom (Sections 2.1.4 – 2.1.5), after which we measured both the reference and 3-d printed phantoms to assess the geometric printing accuracy (Section 2.1.6). To investigate the use of gypsum material as a model for bone, we 3-d printed slabs of this material at a range of infill densities (Section 2.2). In order to understand the dosimetric properties of the gypsum slabs, we measured the WET as a 10-cm square 121.8-MeV proton beam passing through each slab (Section 2.2.2).

2.1 Pediatric Phantom

2.1.0 Reference Geometry

The reference geometry for this study was a commercial anthropomorphic phantom of a 10-year-old child (CIRS, model 703, Norfolk, VA, United States). The phantom comprises a head and torso ending below the hips; it does not include arms or legs. The phantom is divided into thirty-two horizontal segments. Each segment is the appropriate density for its location in the body and is covered by a grid of holes (Figure 1b) for dosimetry tool insertion. When

dosimetry tools are not being used, the holes are filled with plugs matching the density of the surrounding area (i.e., soft tissue, bone, cartilage, spinal cord, lung, or brain) (Figure 1c).

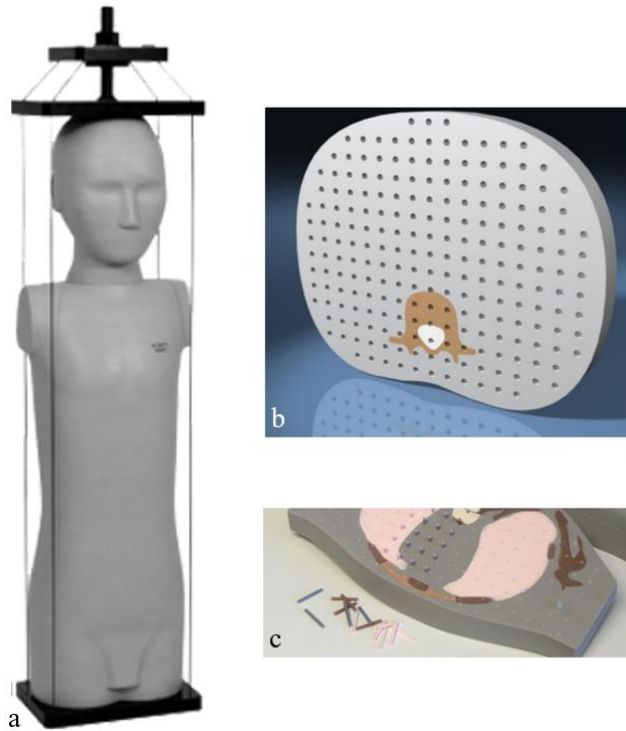


Figure 1 - Reference Phantom (CIRS, model 703, Norfolk, VA, United States). (a) Full phantom¹. (b) Representative example of one segment, showing the grid pattern¹. (c) Representative example of the different tissue-equivalent plugs¹.

2.1.1 Scanning

We scanned the reference geometry (Section 2.1.0) using a full-body scanner (SizeStream, SS20 Classic, Cary, NC, United States). Because the reference phantom lacked limbs, we supported the torso with PVC pipes to simulate legs and used our arms (held on either side of the phantom) to ensure that the anatomy was recognizable in the scanner. Post-processing of the data involved applying a polygon mesh to the scan of the phantom.

2.1.2 Creating Print Instructions

We cropped out the PVC pipes and arms and smoothed the polygon mesh using commercially available software (Rhino 6.0, Rhinoceros 3D, Seattle, WA, United States). The

mesh was exported to a Standard Tessellation Language (STL) file and imported into a slicing software to create the printing instructions (Ultimaker Cura, 3.6.0, Geldermalsen, Gelderland, Netherlands). The reference phantom had a height of $81.4 \text{ cm} \pm 0.1 \text{ cm}$, while the maximum printable height of the 3-d printer utilized in this study was 40 cm (Crealitty 3D, CR-10S, Shenzhen, China). Therefore, we segmented the phantom into three separate prints (Figure 2): a lower torso segment up to the waist, an upper torso segment up to the shoulders, and the head.

2.1.3 Printing the Phantom

We printed the phantom in the three separate sections using polylactic-acid (PLA) printing filament (3D Solutech, 1.75mm PLA filament, Seattle, WA, United States). The walls of each segment were printed 3.0-mm thick and the top of the head and bottom of the torso were printed 9.0-mm thick. Because the phantom would be filled with water, it was printed at 0% infill. The layer height of the print was 0.2 mm and the entire phantom was printed at 220°C .

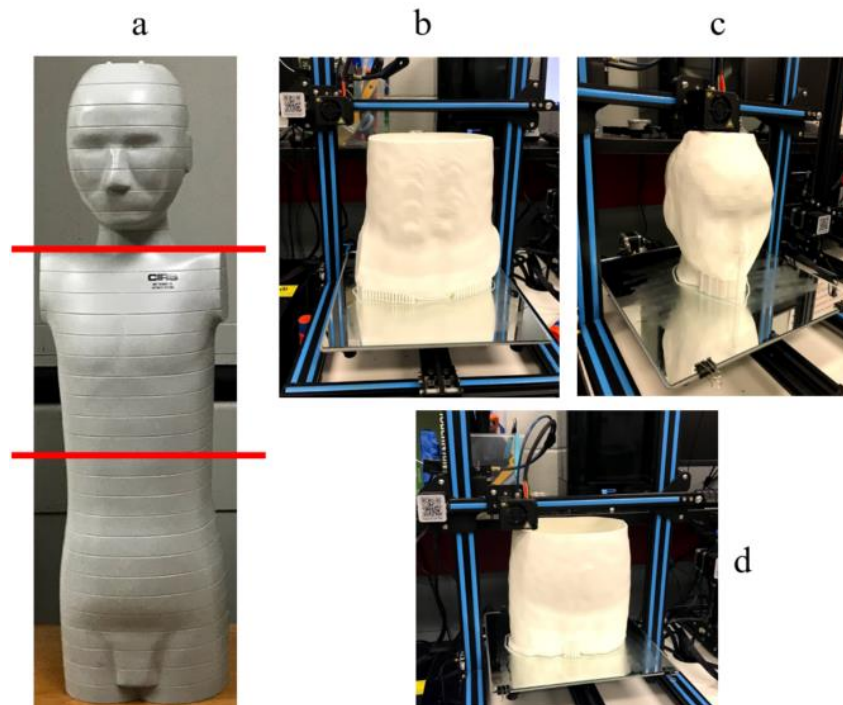


Figure 2 - Segmentation and Printing of the Phantom. (a) Schematic of phantom segmentation where the red lines indicate the locations of the segmentation performed on the scan of the reference phantom for printing. Representative examples of the printing of the (b) upper torso, (c) head, and (d) lower torso, respectively.

2.1.4 Connecting Phantom Segments

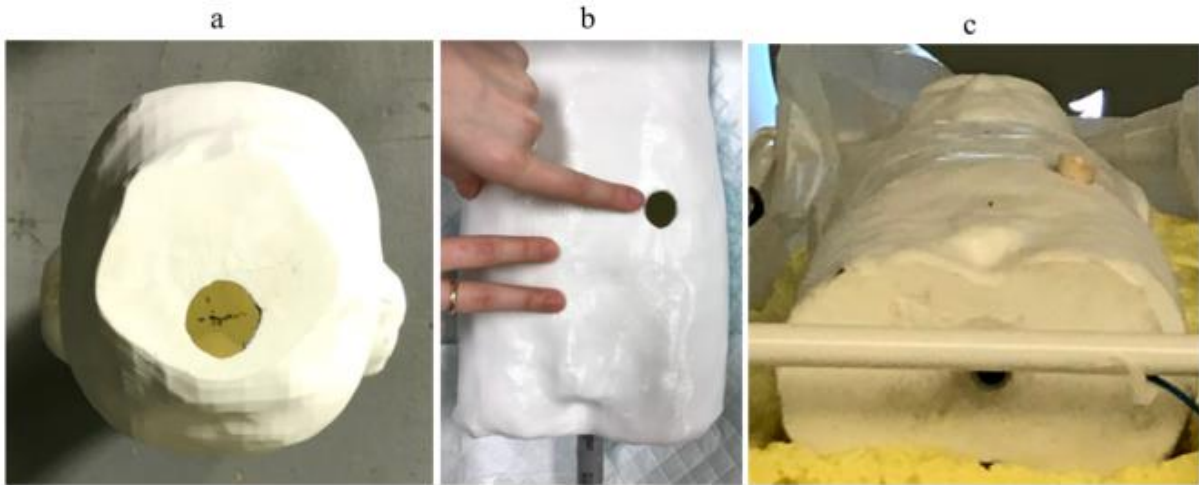





Figure 3 - (a) Positioned above the phantom head, the hole for the conduit was cut where the suture joining the parietal bones. (b) The single finger indicates the hole that was cut for water insertion into the phantom. (c) Positioned at the bottom of the phantom, the hole in the base that allows exit of the conduit is visible. The cork is also placed in the hole from b in this image.

We connected the three separately printed segments and patched holes in the prints using filament and multiple heating tools (Table 1). After welding the phantom pieces together, we cut a hole in the top of the head (Figure 3a) and the pelvic floor (Figure 3c). We then placed PVC conduit through both holes and sealed the junctions with silicone caulk (General Electric, All Purpose 100% Silicone, Waterford, NY, United States). The conduit accommodates the placement of dosimetric measurement devices along the longitudinal (superior-inferior) axis of the phantom. An access hole was cut at the highest point in the abdomen (Figure 3b) for filling and draining the phantom of water. During irradiation, this hole was filled with a rubber cork to prevent water from leaking out.

Table 1 – Summary of the different tools used to combine the three prints together (Section 2.1.4). The soldering iron was used to melt the seam between two segments (Apex Tool Group, Weller WTCPT, Sparks, MD, United States). The heat gun and smoothing head attachment were used with filament to strengthen the seam between segments (Steinel, HL 2010 E, Curtea de Argeş, Romania). The rotary tool was used to seal any holes in the prints (Dremel Europe, model 300, Breda, Netherlands).

Tool Name	Image
<p style="text-align: center;">Soldering Iron (Apex Tool Group, Weller WTCPT, Sparks, MD, United States)</p>	 <p style="text-align: center;">https://www.parts-express.com/weller-wtcpt-soldering-iron-station--372-140</p>
<p style="text-align: center;">Heat Gun and Smoothing Head Attachment (Steinel, HL 2010 E, Curtea de Argeş, Romania)</p>	
<p style="text-align: center;">Rotary Tool (Dremel Europe, model 300, Breda, Netherlands)</p>	

2.1.5 Water-Proofing the Phantom

To waterproof the phantom, we applied a layer of clear sealant and allowed it to dry for twelve hours (Sashco, Through the Roof Sealant, Brighton, UT, United States). We performed a leak test on the phantom by filling the phantom with water and observing its ability to hold that water for 1.5 hours. We performed this test on absorbent pads (Gardnerpet, Puppy Pee Pads, West Bend, WI, United States) that changed color when wet, thereby identifying any leaks. We applied additional sealant to any identified leaks (Liquid Nails, Clear Seal All-Purpose Sealant, Strongsville, OH, United States). After allowing the sealant 1 hour to dry, we repeated the leak test until the phantom held water for 1.5 hours without leaking.

2.1.6 Evaluating the Print Accuracy

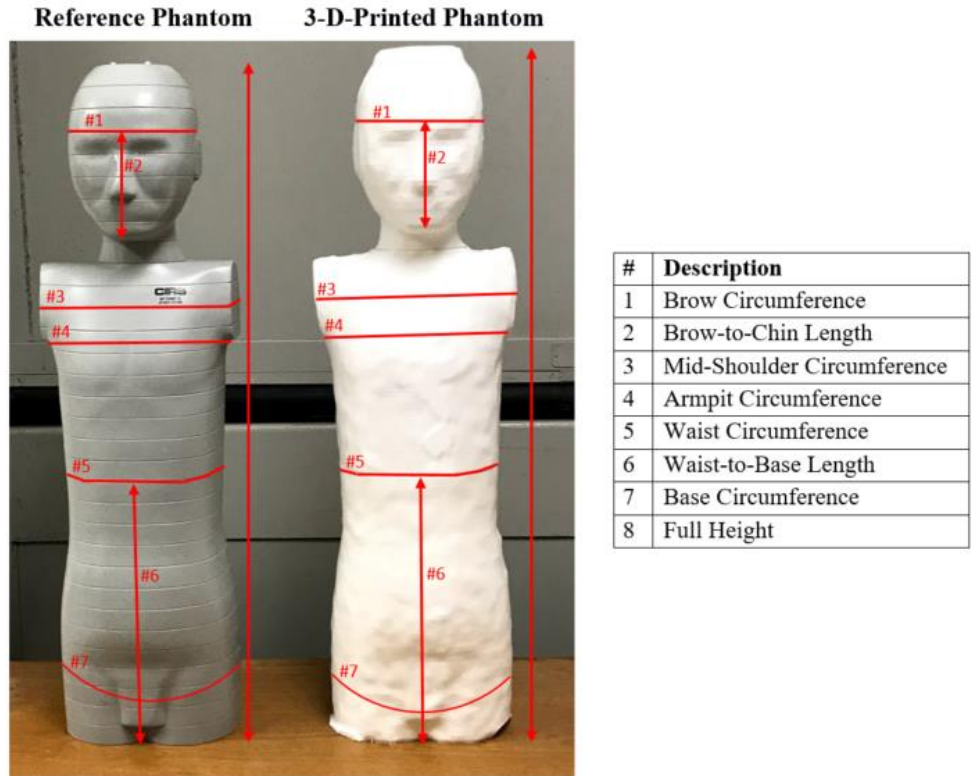


Figure 4 – Locations measurements were taken on the reference phantom (left) and 3-d printed phantom (right) to determine dimensional accuracy of the 3-d-printed phantom.

We measured the dimensional accuracy at various points on both the 3-d-printed and reference phantoms using a tape measure. Eight different positions along the phantom were selected to be easily replicable (Figure 4). We repeated the measurement at each position three times. We then evaluated the accuracy of the print by directly comparing the measurements of the 3-d-printed phantom to those of the reference phantom.

2.2 Bone Heterogeneities

2.2.1 Modeling and Printing the Bone Slabs

In order to assess the potential for a more personalized phantom by the inclusion of a bone model, we 3-d printed using gypsum powder, which is believed to be similar to $\text{CaSO}_4 \cdot$

2H₂O. The exact composition of the powder is a trade secret, however, and therefore not known by us. We 3-d printed slabs of varying infill percentages (i.e., 100%, 85%, 55%, and 70%). These infill percentages correspond to the mass densities 1.39 g/cm³, 1.40 g/cm³, 1.41 g/cm³, and 1.42 g/cm³, respectively. The slabs were modeled as solid blocks using a modeling program (Autodesk, Tinkercad, San Rafael, CA, United States), and we applied a rectilinear infill pattern using a slicing program (Ultimaker, Ultimaker Cura, 3.6.0, Geldermalsen, Gelderland, Netherlands). We varied the infill percentages using the same slicing program. The slab designs were exported to STL files that were then sent to the gypsum 3-d printer (3DSystems, Zprinter 450, Rock Hill, SC, United States).

2.2.2 Evaluation of the Effects of 3-d Printed Gypsum on Range

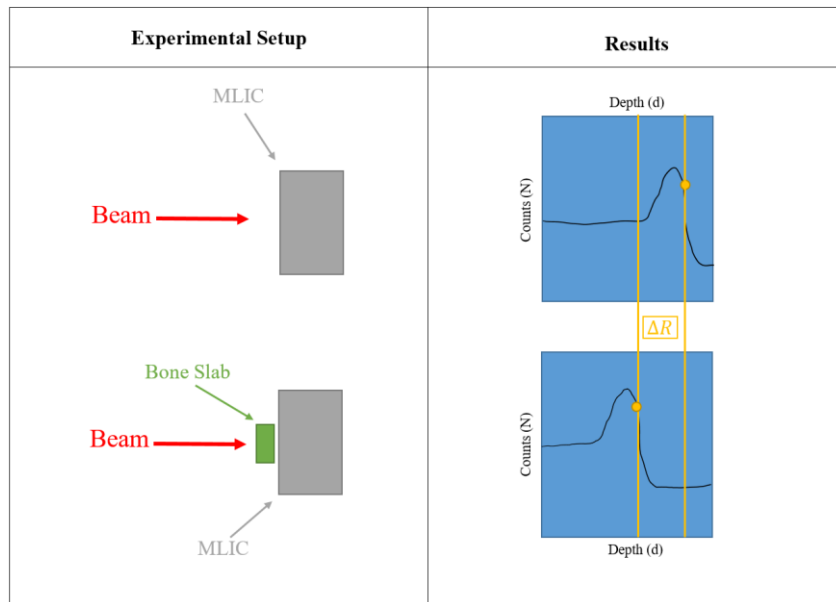


Figure 5 – Schematic diagram representation of the experimental setup and data analysis for testing the properties of the gypsum bone slabs. Tests were performed with a 121.8 MeV proton beam and for each individual bone slab. The blue graphs depict the measured Bragg peaks under reference and test conditions and ΔR represents the range shift in the presence of the bone slab.

As illustrated in Figure 5, the printed gypsum slabs were placed in front of a multi-layer ion chamber (MLIC) as a 121.8-MeV proton beam was sent through the slab (Figure 5) (Zebra, Ion Beam Applications, Louvain-la-Neuve, Belgium). We also performed a reference

measurement without a gypsum slab present. We plotted the Bragg peak for each measurement condition by graphing the measured counts *versus* depth (Figure 6).

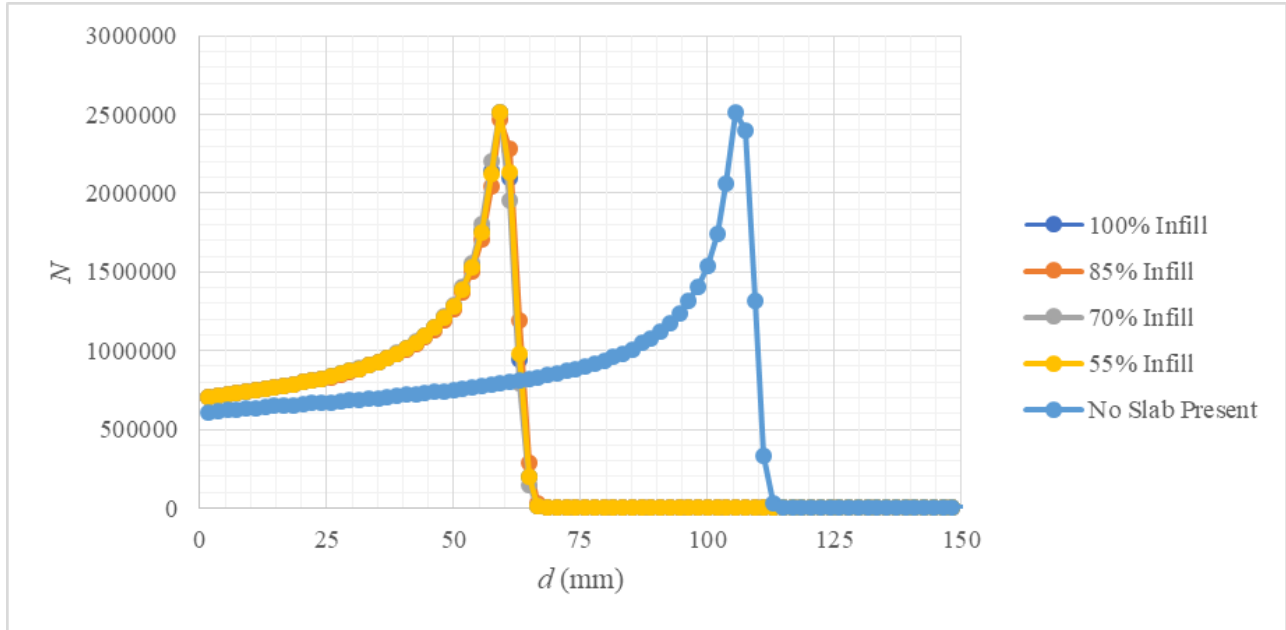


Figure 6 - Plot of the number of counts recorded (N) *versus* depth (d) resulting from a 121.8-MeV proton beam traversing gypsum slabs of varying infill densities.

To determine the water equivalent thickness (WET) of the gypsum, we determined the range difference between the measurements completed with and without the slab present. We defined the range difference as the distance between the distal 80% of the maximum signal of the two peaks. To locate the position of the distal 80% of the maximum signal, we fit an empirical Gaussian to a region of the measured Bragg peaks, *i.e.*,

$$f = \frac{A}{\sigma\sqrt{2\pi}} e^{-\frac{(d-\mu)^2}{2\sigma^2}} \quad 1$$

where f is the signal strength, σ is the width parameter of the Bragg peak, A is the magnitude, d is the depth, and μ is the average of the Gaussian peak. We fit Equation 1 in the region between the proximal 80% to the distal 10%, relative to the maximum signal, using a commercial optimization tool (Excel, Microsoft, Redmond, WA, United States). The depth of the distal 80% of the maximum signal was found using

$$d_{80} = \sqrt{-2\sigma^2 \ln\left(\frac{f\sigma\sqrt{2\pi}}{A}\right)} + \mu \quad 2$$

where d_{80} is depth at the distal 80% of the maximum signal, f is the signal strength at 80% of the maximum signal (as measured by the Gaussian fit), σ is the width parameter of the Bragg peak, A is the magnitude, and μ is the average of the Gaussian peak. In order to find the measured WET of the gypsum slabs, we calculated

$$t_{w,m} = d_{80,ns} - d_{80,s} \quad 3$$

where $t_{w,m}$ is the measured WET of one gypsum slab, $d_{80,ns}$ is the depth at 80% of the maximum signal when no slab was present, and $d_{80,s}$ is the depth at 80% of the maximum signal when one slab was present. We then compared this measured range shift, $t_{w,m}$, to corresponding theoretical values.

Using the methods of Zhang and Newhauser²¹, we calculated the theoretical water-equivalent thickness (WET) of each bone slab as

$$t_w = t_m \frac{\rho_m \bar{S}_m}{\rho_w \bar{S}_w} \quad 4$$

where t_w is the WET of the slab, t_m is the geometric thickness of the slab, ρ_m and ρ_w are the mass densities of the slab and water, respectively, and \bar{S}_m and \bar{S}_w are the mean proton mass stopping power values for the slab and water, respectively. Stopping powers from Ziegler *et al.* were used for these calculations²². The mean proton mass stopping powers were found using

$$\bar{S} \approx S(\bar{E}) \approx S\left[\frac{E_0 - \Delta E}{2}\right] \quad 5$$

where \bar{S} is the mean proton mass stopping power, \bar{E} is the mean energy, E_0 is the initial beam energy, and ΔE is the energy lost by the beam in the slab. ΔE was calculated as

$$\Delta E \approx S(E_0) * \rho_m * t_m$$

where $S(E_0)$ is the mass stopping power of the material evaluated at the initial proton beam energy E_0 , ρ_m is the mass density of the material, and t_m is the thickness of the material. After calculating the theoretical WET of each gypsum slab using Equation 4, we compared these to the measured WET value for each slab. We also compared the measured WET value for each slab to the theoretical WET values for human cortical bone, which were calculated using the same method.

Chapter 3

Results

3.1 Geometric Accuracy of Whole Body Phantom

Table 2 lists the results of the geometric measurements of the reference and 3-d-printed pediatric phantoms. Overall, there was a small standard deviation of the mean in both the 3-d printed and reference phantom measurements of 0.5-mm and 0.4-mm on average, respectively. Therefore, the two phantoms have almost equal uncertainties.

Table 2 - Measurements of the 3-d-printed and reference phantoms. Data include the results of each of 3 measurements at each measurement location (i.e., M1, M2, and M3) as well as the average (\bar{M}) and standard deviation of the mean (SE). Measurements were performed at the same eight locations on both phantoms.

Location of Measurement	3-D Printed Phantom					Reference Phantom				
	M1	M2	M3	\bar{M}	SE	M1	M2	M3	\bar{M}	SE
Brow Circumference (cm)	52.5	52.6	52.4	52.5	0.06	52.3	52.3	52.2	52.3	0.03
Brow-to-Chin Length (cm)	11.9	12.0	11.9	11.9	0.03	11.7	11.9	11.8	11.8	0.06
Mid-Shoulder Circumference (cm)	64.5	64.4	64.4	64.4	0.03	63.9	64.0	64.0	64.0	0.03
Armpit Circumference (cm)	62.6	62.4	62.2	62.4	0.12	61.4	61.5	61.4	61.4	0.03
Waist Circumference (cm)	58.1	58.0	58.1	58.1	0.03	57.6	57.7	57.6	57.6	0.03
Waist to Base Length (cm)	33.7	33.8	33.8	33.8	0.03	33.3	33.2	33.2	33.2	0.03
Base Circumference (cm)	59.4	59.3	59.4	59.4	0.03	59.1	59.1	59.1	59.1	0.00
Full Height (cm)	82.2	82.3	82.5	82.3	0.09	81.4	81.5	81.3	81.4	0.06

Table 3 lists the absolute difference in dimensions ($\Delta\bar{M}$) between the reference and 3-d-printed phantoms at each measurement location, calculated as,

$$\Delta\bar{M} = \bar{M}_{printed} - \bar{M}_{reference} \quad 7$$

where $\bar{M}_{printed}$ and $\bar{M}_{reference}$ are the average dimensions for the 3-d-printed and reference phantoms, respectively. We quantified the uncertainty in $\Delta\bar{M}$ using standard error-propagation methods. This table shows that the 3-d-printed phantom was dimensionally larger than the reference phantom at each measurement location. According to these results, the measurement locations with the largest dimensional differences were the armpit circumference and the full height, which differed by (1.0 ± 0.1) cm and (0.9 ± 0.1) cm, respectively. Table 3 also lists the ratio of the measurements from the 3-d-printed phantom to those from the reference phantom at each location, which is also plotted in Figure 7. These data illustrate that all of the measured dimensions of the 3-d-printed phantom differed from the reference phantom by no more than $0.97 \text{ cm} \pm 0.12 \text{ cm}$ and were within $1.6\% \pm 0.2\%$ of the reference geometry (Figure 7).

Table 3 - Quantification of the dimensional accuracy of the 3-d-printed phantom. Data include the absolute difference between the dimensions of 3-d-printed and reference phantoms ($\Delta\bar{M}$) at each measurement location and its uncertainty ($\sigma_{\Delta\bar{M}}$) as well as the ratio of the average dimensions of 3-d-printed to reference phantoms ($\Delta\bar{M}_{ratio}$) at each measurement location and its uncertainty of the ratio ($\sigma_{\Delta\bar{M}_{ratio}}$).

Location	$\Delta\bar{M}$ (cm)	$\sigma_{\Delta\bar{M}}$ (cm)	$\Delta\bar{M}_{ratio}$ (3-D/ref)	$\sigma_{\Delta\bar{M}_{ratio}}$
Brow Circumference	0.23	0.07	1.004	0.001
Brow to Chin Length	0.13	0.07	1.011	0.006
Mid Shoulder Circumference	0.47	0.05	1.007	0.001
Armpit Circumference	0.97	0.12	1.016	0.002
Waist Circumference	0.43	0.05	1.008	0.001
Waist to Base Length	0.53	0.05	1.016	0.001
Base Circumference	0.27	0.03	1.005	0.001
Full Height	0.93	0.11	1.011	0.001

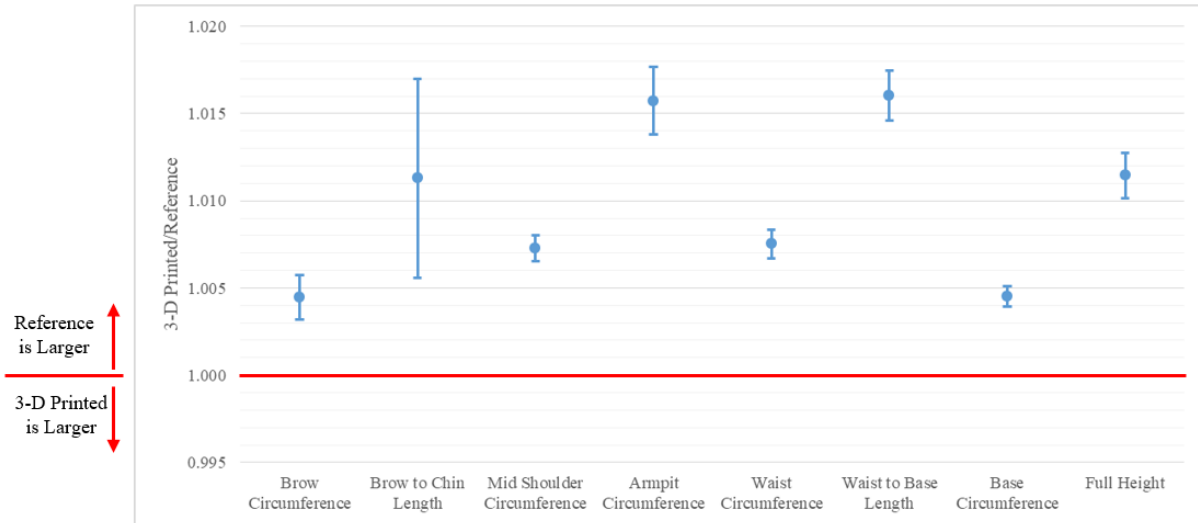


Figure 7 - Graph of the Ratio of Measurements of the 3-D-Printed Phantom to the Reference Phantom ($\Delta\bar{M}_{ratio}$, see Table 3). The average measurements for each phantom at each position were used to graph the ratio of the measurements in the 3-d printed and reference phantoms. A ratio equal to 1 indicates that the phantoms are statistically equal, and this is indicated by the red line on the graph. A ratio of less than 1 indicates that the reference phantom is larger, and a ratio of greater than 1 indicates that the 3-d-printed phantom is larger.

3.2 Dosimetric Accuracy of Bone Heterogeneities

Table 4 lists the results of the tests for 3-d printed gypsum slabs as a bone substitute.

This table reveals that, unexpectedly, the mass densities of the slabs did not vary according to infill pattern. Instead, our results indicate that our methods were not effective for varying the infill pattern in gypsum printing. This was evidently due to limitations of the printer's ability to create infill patterns using the binder jetting printing technique.

The binder jetting printing method involves a series of steps that are repeated for every layer of the print. The printer operates by first creating a layer of powder (3D Systems, zp131, Rock Hill, SC, United States) upon which the print will be built. Next, the inkjet print head prints the binder (3D Systems, zb63, Rock Hill, SC, United States) in the specified print pattern, which in our case was the infill pattern. After one layer of binder (3D Systems, zb63, Rock Hill, SC, United States) has been printed, the printer wipes a thin layer of powder (3D Systems, zp131, Rock Hill, SC, United States) across the print. This process is then repeated on the new

layer of powder (3D Systems, zp131, Rock Hill, SC, United States). Because the printer wipes a layer of powder across the print before completing the next layer of the print, however, there is not a way for the spaces between the infill patterns being printed to remain empty. Instead, the spaces are filled with powder when the printer wipes a new layer of powder across the print, which results in a lack of density variation between slabs. Therefore, attempting to vary infill density in a binder jetting 3-d printer is not plausible.

Table 4 - Results of bone-substitute slab tests. Data include the 3-d-printing infill percentage, shift in Bragg-peak depth between test and reference conditions, $t_{w,m}$, calculated WET of the gypsum slabs $t_{w,c}$, absolute difference in the gypsum WET values, Δt_w , ratio of the WET values, and the physical density of the gypsum slabs as well as water, ρ_m and ρ_w , respectively.

Slab Infill %	$t_{w,m}$	$t_{w,c}$	Δt_w	$\frac{t_{w,m}}{t_{w,c}}$	t_m	ρ_m	ρ_w	$(dE/\rho dx)_m$	$(dE/\rho dx)_w$
Units	[mm]	[mm]	[mm]	unitless	[mm]	$\left[\frac{g}{cm^3}\right]$	$\left[\frac{g}{cm^3}\right]$	$\left[\frac{MeV \cdot cm^2}{g}\right]$	$\left[\frac{MeV \cdot cm^2}{g}\right]$
100	46.96	41.16	5.79	1.141	30	1.578	1.0	5.954	6.848
85	46.51	41.68	4.83	1.116	30	1.598	1.0	5.961	6.856
70	47.20	41.76	5.44	1.130	30	1.601	1.0	5.962	6.857
55	46.89	41.81	5.07	1.121	30	1.603	1.0	5.963	6.858

Similarly, the data listed in Table 4 reveals that the Bragg peaks of proton beams traversing each slab did not vary much from one another. There was, as expected, a consistent range shift caused by the presence of the slab, $t_{w,m}$. The average shift between the measurements with slabs and the measurement without a slab present was $46.9 \text{ mm} \pm 0.1 \text{ mm}$ (WET).

Table 4 lists both the measured WET for each block, $t_{w,m}$, and the calculated WET for each slab, $t_{w,c}$. These measured and calculated WET values for each slab differ on average by $12.71\% \pm 0.01\%$. We assumed that the gypsum slabs were produced using pure gypsum, however, because of the proprietary nature of the powder, we do not know its exact chemical composition. One possible explanation for the discrepancy between measured and calculated WET values for the gypsum slabs is the possible presence of a high-Z element, which would

result in a higher material stopping power, and ultimately a larger WET closer to what we measured for the gypsum slabs.

Table 5 – Results of shift in Bragg-peak depth between test and reference conditions, $t_{w,m}$, and the published WET values for cortical bone²², $t_{w,b}$, under the same conditions.

Slab Infill %	$t_{w,m}$ [mm]	$t_{w,b}$ [mm]	Mean CT Value (HU)
100	46.96	49.94	819
85	46.51	49.94	850
70	47.20	49.94	855
55	46.89	49.94	857

According to Table 5, the values we reported for the WET of the gypsum slabs, $t_{w,m}$, are similar to the calculated WET values for cortical bone (Section 2.2.2) under the same conditions. On average, the measured WET values of the slabs varied from the WET values of cortical bone by $6.5\% \pm 0.3\%$.

Chapter 4

Discussion

In this study, we replicated an anthropomorphic reference phantom using optical 3-d scanning and fused deposition modeling 3-d printing. We also utilized binder jetting 3-d printing to fabricate a bone substitute slab. The major finding of this work was that it is possible to create 3-d printed phantoms with dimensional accuracy within $0.97\text{ cm} \pm 0.12\text{ cm}$ and $1.6\% \pm 0.2\%$ of a reference geometry and it is possible to use 3-d printed gypsum as a bone substitute material. Therefore, the results of this work suggest that it will become feasible to print a life-sized personalized phantom with a high degree of dimensional accuracy and utilize gypsum as a dosimetric bone substitute material.

The results of this study indicate that previous concerns of the potential for defects caused by limitations of the scanning and/or printing methods (*e.g.* gravity-induced deformations during cooling) may be overcome. This new knowledge can aid in the eventual shift towards more personalized treatment approaches for patients with abnormal anatomies. Although the current gypsum printing methods didn't allow for varying infill percentage, it seems likely that this technical limitation can be overcome in the future. Together, the results of this study suggest that with further research and development, heterogeneous phantoms of individual patients could be printed for use in a clinical setting.

The results of this study are consistent with related studies in the literature. 3-D printing with FDM is a popular technique in the literature^{6, 8-10, 12-14, 17, 23, 24}. The most comparable study of the dimensional accuracy of 3-d-printed phantoms was that of Craft and Howell who 3-d printed the upper torso of a mastectomy patient using FDM with PLA filament⁶. Craft and Howell observed an overall increased size between their 3-d-printed phantom and the planned model; on average, the dimensional error for each 3-d printed slice was 0.52-mm. These results are in agreement with our findings that the 3-d-printed phantom was consistently larger than the reference. Our 3-d printed phantom was, however, printed with a lower dimensional accuracy, varying from the reference phantom by an average of 5-mm. In the most comparable study involving 3-d printed bone models, Mayer *et al.* 3-d printed the thorax of a patient using a photopolymer polyjet printing material (Stratasys, VeroWhite, Rehovot, Israel) for the bone material¹⁸. Their findings showed that this material (Stratasys, VeroWhite, Rehovot, Israel) was lower on the Hounsfield scale than bone, measuring 136 HU compared to the 200-1000 HU-range of bone¹⁸. The gypsum slabs that we printed measured higher on the Hounsfield scale than the photopolymer polyjet printing material used by Mayer *et al.* (Stratasys, VeroWhite, Rehovot,

Israel), with an average of 845 HU (Table 5), and therefore, gypsum was more similar radiographically to bone than this material (Stratasys, VeroWhite, Rehovot, Israel)¹⁸.

This study has several strengths. To begin with, we used two very common 3-d printing techniques—FDM and binder jetting. FDM is a widespread printing method due to its print material strength, low cost, and ease of use¹⁴. Binder jetting is a great printing option for complex geometries because it does not require support materials due to the powder support during printing¹⁴. Another major strength of this study was that we tested the end-to-end feasibility of creating a 3-d printed phantom. This entire process consisted of the many different phases beginning with scanning (Section 2.1.1) and creating the print instructions (Section 2.1.2), then printing (Section 2.1.3) and post-processing (Section 2.1.4), and finally waterproofing (Section 2.1.5). This comprehensive review of creating a 3-d printed anthropomorphic phantom allows for reproducibility and further study of 3-d printing for dosimetric purposes. Finally, we studied two aspects of the 3-d printing we performed—both dimensional (Section 2.1.6) and dosimetric (Section 2.2.2) accuracy. This provided feedback on both the achieved printing accuracy of the phantom as well as the dosimetric accuracy of using 3-d printed gypsum slabs as a substitute for bone.

This study had several limitations. First was the simplicity of the measurement technique that we used to analyze the consistency of the two phantoms, which involved measuring the dimensions at eight different locations on both the 3-d-printed and reference phantoms. More advanced methods exist enabling increased precision in the dimensional analysis, including measuring the print accuracy by analyzing the volumetric accuracy of the print⁶ or using photogrammetry software (Capturing Reality, RealityCapture, Bratislava, Slovakia) to compare scans of the two phantoms. This was not considered a serious limitation, however, because the

methods we used (Section 2.1.6) were valid; the use of a photogrammetry software would enable more complete and specific dimensional information. Another limitation of this study is that the phantom had to be printed in three prints, rather than in one print on a larger 3-d printer. This process necessitated molding the pieces together, which increased the dimensional error. Nevertheless, we still achieved a high level of dimensional accuracy (*i.e.*, $1.6\% \pm 0.2\%$ and $0.97 \text{ cm} \pm 0.12 \text{ cm}$), which represents an upper bound on the current capabilities of 3-d-scanning and 3-d-printing techniques in this application. Another limitation of this study was the inability to know the exact chemical composition of the gypsum 3-d printing powder (3D Systems, zp131, Rock Hill, SC, United States) due to its proprietary, secret formulation. This was not, however, considered a serious limitation because we were still able to calculate the range shift due to gypsum within $12.71\% \pm 0.01\%$ of the measured values. Furthermore, it is possible to analyze a sample of the material to estimate the elemental mass fractions.

Chapter 5

Conclusion

The results of this study indicate that 3-d printing phantoms within $0.97 \text{ cm} \pm 0.12 \text{ cm}$ and $1.6\% \pm 0.2\%$ of the scanned reference geometry is possible. We also demonstrated that 3-d-printed gypsum is dosimetrically similar to bone and can therefore serve as a bone model. Incorporating this or similar models for tissue heterogeneities enables more accurate measurements of the energy deposition in the phantom. The findings indicate an opportunity for more precise, and therefore improved treatment-planning capabilities for those patients not well-represented by population-averaged phantoms by the use of 3-d-printed, patient-specific phantoms. Together, 3-d printing personalized phantoms and bone modeling using gypsum can be implemented to construct personalized phantoms, complete with accurate geometrical and

dosimetric representation of the patient's anatomical uniqueness. With future research and development, personalized phantoms have the potential to be incorporated into standard clinical protocol for those patients with abnormal anatomies.

References

1. (Computerized Imaging Reference Systems, Inc., Norfolk, VA, 2013), pp. 8, 4.
2. A. Sudhakar, *Journal of cancer science & therapy* **1** (2), 1-4 (2009).
3. in *Disease Control Priorities*, edited by H. Gelband, P. Jha, R. Sankaranarayanan and S. Horton (World Bank, Washington, DC, 2015), Vol. 3.
4. R. Alan Mitteer, Y. Wang, J. Shah, S. Gordon, M. Fager, P.-P. Butter, H. Jun Kim, C. Guardiola-Salmeron, A. Carabe-Fernandez and Y. Fan, *Scientific Reports* **5**, 13961 (2015).
5. W. D. Newhauser and R. Zhang, (2015), Vol. 60, pp. R155-R209.
6. D. F. Craft and R. M. Howell, *Journal of Applied Clinical Medical Physics* **18** (5), 285-292 (2017).
7. A. M. Halloran, Louisiana State University, 2015.
8. T. Kamomae, H. Shimizu, T. Nakaya, K. Okudaira, T. Aoyama, H. Oguchi, M. Komori, M. Kawamura, K. Ohtakara, H. Monzen, Y. Itoh and S. Naganawa, *Physica Medica* **44**, 205-211 (2017).
9. C. L. Ventola, *Pharmacy and Therapeutics* **39** (10), 704-711 (2014).
10. E. D. Ehler, B. M. Barney, P. D. Higgins and K. E. Dusenbery, *Patient specific 3D printed phantom for IMRT quality assurance*. (2014).
11. W. Newhauser, C. Schneider, L. Wilson, S. Shrestha and W. Donahue, *A review of analytical models of stray radiation exposures from Photon- and Proton-Beam radiotherapies*. (2017).
12. J. Madamesila, P. McGeachy, J. E. Villarreal Barajas and R. Khan, *Physica Medica* **32** (1), 242-247 (2016).
13. T. D. Ngo, A. Kashani, G. Imbalzano, K. T. Q. Nguyen and D. Hui, *Composites Part B: Engineering* **143**, 172-196 (2018).
14. D. Mitsouras, P. Liacouras, A. Imanzadeh, A. A. Giannopoulos, T. Cai, K. K. Kumamaru, E. George, N. Wake, E. J. Caterson, B. Pomahac, V. B. Ho, G. T. Grant and F. J. Rybicki, *RadioGraphics* **35** (7), 1965-1988 (2015).
15. S. Fereshtenejad and J.-J. Song, *Rock Mechanics and Rock Engineering* **49** (6), 2065-2074 (2016).
16. R. Zhang, P. J. Taddei, M. M. Fitzek and W. D. Newhauser, *Physics in medicine and biology* **55** (9), 2481-2493 (2010).
17. C. Hazelaar, M. Eijnatten, M. Dahele, J. Wolff, T. Forouzanfar, B. Slotman and W. F. A. R. Verbakel, *Medical Physics* **45** (1), 92-100 (2018).
18. R. Mayer, P. Liacouras, A. Thomas, M. Kang, L. Lin and C. B Simone, *3D printer generated thorax phantom with mobile tumor for radiation dosimetry*. (2015).
19. R. Bibb, D. Thompson and J. Winder, *Medical Engineering & Physics* **33** (5), 590-596 (2011).
20. M. Moore and W. D. Newhauser, (in preparation).
21. R. Zhang and W. D. Newhauser, *Phys Med Biol* **54** (6), 1383-1395 (2009).
22. J. F. Ziegler, J. P. Biersack and M. D. Ziegler, *SRIM : The Stopping and Range of Ions in Matter*. (SRIM Co., Chester, Md., 2012).
23. J. Wu, N. Aage, R. Westermann and O. Sigmund, (2016).
24. S. Burlinson, J. Baker, A. T. Hsia and Z. Xu, *Journal of Applied Clinical Medical Physics* **16** (3), 166-178 (2015).